PHYSICAL REVIEW B **113**, 155405 (2026)

Kagome bands and magnetism in MoTe_{2-x} kagome monolayers

Jiaqi Dai,[1,2,*] Zhongqin Zhang,[1,2,*] Zemin Pan,[3,4] Cong Wang,[1,2] Chendong Zhang,[3,4,†] Zhihai Cheng,[1,2] and Wei Ji[1,2,‡]
[1]*Beijing Key Laboratory of Optoelectronic Functional Materials & Micro-Nano Devices, School of Physics, Renmin University of China, Beijing 100872, China*
[2]*Key Laboratory of Quantum State Construction and Manipulation (Ministry of Education), Renmin University of China, Beijing 100872, China*
[3]*School of Physics and Technology, Wuhan University, Wuhan 430072, China*
[4]*Wuhan Institute of Quantum Technology, Wuhan 430206, China*

(Received 29 April 2025; revised 11 February 2026; accepted 23 February 2026; published 3 April 2026)

Kagome lattices facilitate various quantum phases, yet in bulk materials, their kagome flat bands often interact with bulk bands, suppressing kagome electronic characteristics for hosting these phases. Here, we use density functional theory calculations to predict the geometric and electronic structures as well as the topological and magnetic properties of a series of MoTe_{2-x} kagome monolayers formed by mirror-twin-boundary (MTB) loops. We analyze 13 MTB-loop configurations of varying sizes and arrangements to assess their impacts on various properties. Within the intrinsic band gap of MoTe_2, we identify two sets of kagome bands, primarily originating from in-plane and out-of-plane Mo d orbitals at MTB-loop edges and vertices, respectively. Four configurations exhibit superior stability in certain ranges of Te chemical potentials, respectively, while others show comparable stability. Among these configurations, four display band gaps and potentially nonzero Z_2 topological invariants, suggesting possible topological phases, while the remaining two are metallic and feature Stoner magnetization. These findings guide the design of kagome-based two-dimensional materials with tunable electronic, topological, and magnetic properties.

DOI: 10.1103/tmd3-whft

I. INTRODUCTION

Kagome materials have attracted significant attention for their electronic properties, such as flat bands, Dirac cones, and Van Hove singularities [1,2]. These features enable diverse quantum phases such as magnetism [3,4], superconductivity [5,6], and charge density waves (CDWs) [7,8], making the kagome lattice a prime candidate for studying correlated and topological electronic phenomena [1,2,4,9]. While bulk kagome materials exhibit intriguing properties [1,2,5,10], such as the magnetic Weyl semimetal phase in $\mathrm{Co_3Sn_2S_2}$ [4,11–13] and superconductivity in $A\mathrm{V_3Sb_5}$ (A = alkali metals) [5,14], their electronic structures are often complicated by coupling with capping layers [4,15–17]. This coupling causes characteristic kagome bands, like flat bands, to mix up with other bulk bands [4,15] and often to be placed away from the Fermi levels [16,17]. Consequently, direct tuning the filling factors of electronic flat bands or Van Hove singularities, essential for accessing quantum phases, is challenging in bulk materials.

Two-dimensional (2D) kagome materials offer a promising solution to these challenges. Inherently stable without capping layers, they effectively suppress couplings between kagome bands and bulk states. Their reduced thickness also lowers carrier densities, facilitating the experimental tuning of filling factors of kagome bands. However, exfoliating 2D kagome materials from their bulk counterparts is difficult due to their non-van der Waals (vdW) interlayer interactions [12,13,18]. Even for recently reported vdW kagome materials like $\mathrm{Nb_3Cl_8}$, successful exfoliation of its monolayer remains challenging [2,19]. Twisted moiré bilayers can host electronic kagome lattices [20–24] but introduce complications such as structural reconstructions [25–27] and issues on stability and scalability [28–32]. While monolayer kagome materials show potential [1,2,33–35], achieving and maintaining stable structures with desirable properties remains difficult. Progress has been made in constructing kagome monolayers on metal surfaces using organic molecules [36] or inorganic clusters [37], but the resulting kagome-like band structures often arise from interactions with substrates [37–40] rather than intrinsic kagome bands. These issues persist across other approaches, like surface adatoms [41–43], intercalation [44,45], hybridization [46], and molecular manipulation [47]. Therefore, innovative strategies are necessitated to build 2D kagome lattices nearly decoupled from the substrates [48].

Monolayer $\mathrm{MoTe_2}$ [33,49,50] and its analogs, such as $\mathrm{MoSe_2}$ [51–53], contain mirror twin boundaries (MTBs) [33,49–53] that lead to polymorphic phases [33,49,50]. These MTBs induce two defect states with the band gap of the parent MoTe monolayer, substantially isolating them from other bulk states [51,53], as illustrated in Fig. S1 in the Supplemental Material [54]. Here, we predict a series of MoTe_{2-x} kagome monolayers with varying MTB-loop sizes and arrangements using density functional theory (DFT) calculations. We established the relationship between MTB-loop configurations

---

[*] These authors contributed equally to this work.
[†] Contact author: cdzhang@whu.edu.cn
[‡] Contact author: wji@ruc.edu.cn

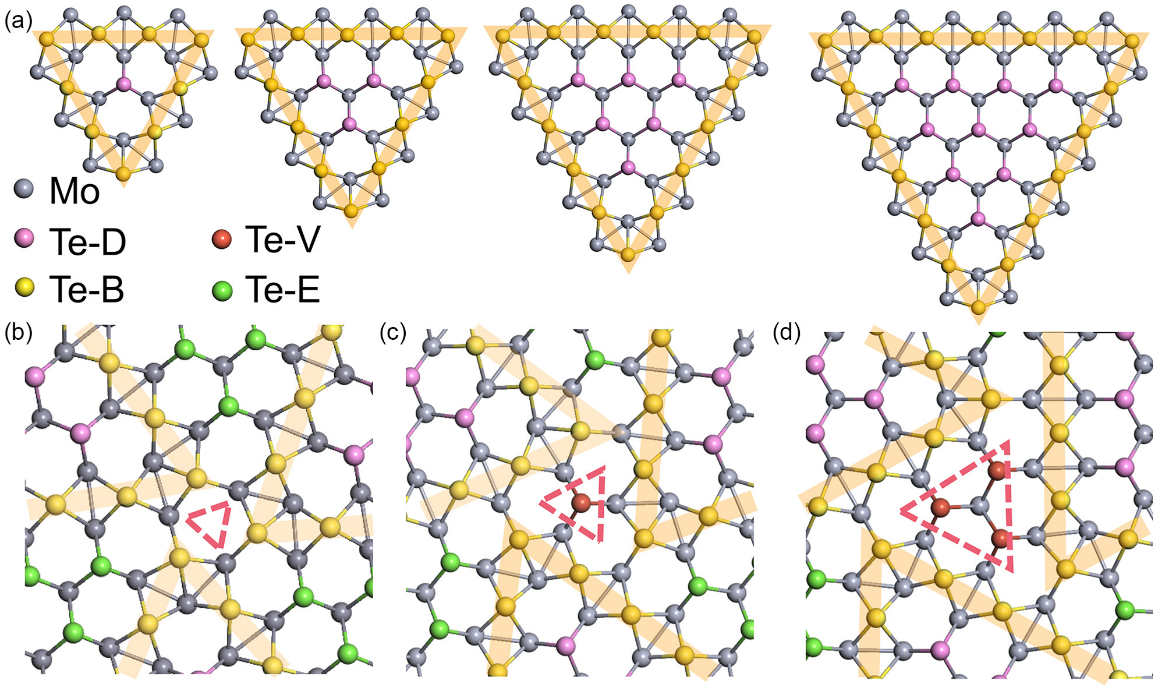

FIG. 1. Size and arrangement of triangular MTB loops in $MoTe_{2-x}$ monolayers. (a) Atomic models of triangular MTB loops with $N = 1, 3, 6$, and 10 (from left to right). Light orange triangles highlight the MTBs. Pink, yellow, red, and green balls represent Te_2 dimers located inside the triangular MTB loops (Te_2-D), on the MTB boundaries (Te_2-B), among the vertices (Te_2-V), and surrounded among the edges (Te_2-E), respectively. Slate blue balls represent Mo atoms. Atomic models of the (b) $T0$, (c) $T1$, and (d) $T3$ arrangements in $MoTe_{2-x}$ monolayers. Red dashed lines outline the triangles surrounded by MTB vertices.

and their resulting electronic structures near the Fermi level. Among 13 configurations, we observed topological flat bands and Dirac states within the band gap of parent monolayer $MoTe_2$, resulting in gapped (metallic) $MoTe_{2-x}$ monolayers. These states lead to ferromagnetism (FM) and potentially quantum spin Hall or correlated insulators.

II. METHODS

Our DFT calculations were performed using the generalized gradient approximation for the exchange-correlation potential in the form of Perdew-Burke-Ernzerhof [55], the projector augmented-wave method [56], and a plane-wave basis set as implemented in VASP [57]. Van der Waals interactions was performed at vdW-DF level for all calculations, with the optB86b functional for the exchange potential [58]. The energy cutoff for the plane-wave basis sets was set to 500 eV for variable volume structural relaxation and electronic structure calculations. All atoms, lattice volumes, and shapes were allowed to relax until the residual force per atom was below 0.01 eV/Å. A vacuum layer exceeding 15 Å in thickness was employed to reduce imaging interactions between adjacent supercells. A Γ-centered k-mesh of $5 \times 5 \times 1$ and $3 \times 3 \times 1$ was used to sample the first Brillouin zone of the unit cell for N1/N3 and N6/N10/N15/N21, respectively. The Gaussian smearing method with a σ value of 0.02 eV was applied for all calculations. By using the WANNIER90 package, we constructed the tight-binding model of $MoTe_2$ with Mo $4d$ and Te $5p$ orbitals based on the maximally localized Wannier functions method [59], performing on DFT calculations with spin-orbit coupling (SOC). We further calculated topological phases with Z_2 invariants using the WANNIERTOOLS software package [60].

Experimental samples were grown on bilayer graphene, which was prepared by heating SiC (0001) in a home-built ultrahigh vacuum molecular beam epitaxy system with a base pressure of approximately 1.0×10^{-10} Torr. Te (99.999%) was evaporated from Knudsen cells, and high-purity Mo (99.95%) was evaporated from an e-beam evaporator, respectively. The flux ratios of Te/Mo were 30. The substrate was kept at approximately 200 °C. The deposition of $MoTe_2$ was followed by a 10 min annealing at the growth temperature with the Te flux maintained. Subsequently, the substrate temperature was increased to 350–500 °C [61] and annealed for 1 h to obtain the various ordered MTB superstructures. The scanning tunneling microscopy (STM) measurements were carried out using a commercial Unisoku 1400 LT-STM system at 4.3 K (base pressure: $<1 \times 10^{-10}$ Torr). Electrochemically etched W-tips were cleaned *in situ* with electron-beam bombardment and used in all measurements.

III. RESULTS

A. Kagome superstructure of $MoTe_{2-x}$

For free-standing H-phase monolayer $MoTe_2$, removal of some Te atoms leads to $MoTe_{2-x}$ monolayers with MTBs, which form distinct triangular loops (highlighted in light orange) essential for constructing MTB superlattices. As shown in Fig. 1(a) and Fig. S2 in the Supplemental Material [54], these loops, varying in size, are the build-

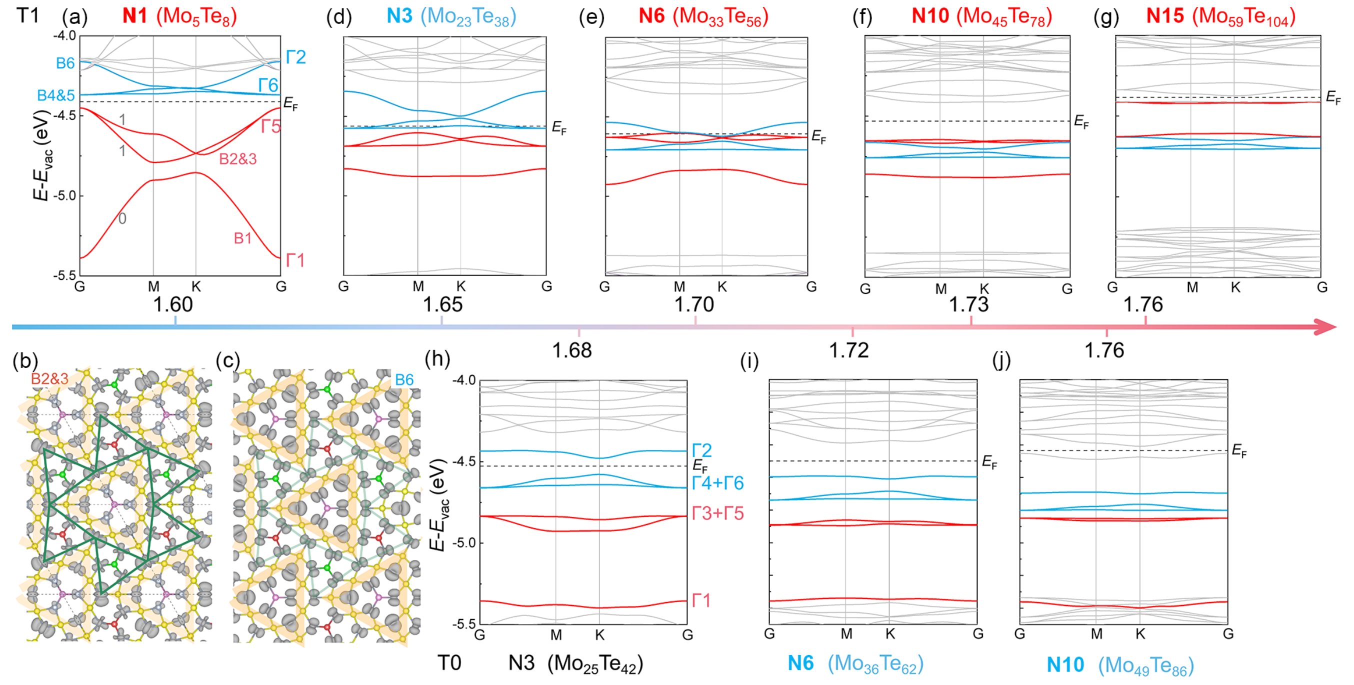

FIG. 2. Band structures of MoTe$_{2-x}$ monolayers with varying sizes and arrangements of MTB loops. (a) Band structure of $N1T1$, in which B1–B6 represent six colored bands in increasing order of energy. Z_2 topological invariants of B1, B2, and B3 are marked with gray numbers in (a). Visualized wave function norms of bands (b) B2 and B3 and (c) B6 at the Γ point. The isosurface contours are 3×10^{-3} e/Bohr^3. Dark green solid lines connect the Mo d_{z^2} orbitals (hybridizing with d_{xy} and $d_{x^2\text{-}y^2}$ orbitals), highlighting a CT lattice in (b). Light-orange shadowed triangles indicate the MTB loops in (b) and (c). (d)–(g) Band structures of nonmagnetic $NxT1$ ($N = 3$, 6, 10, and 15) monolayers. (h)–(j) Nonmagnetic band structures of $NxT0$ ($N = 1$, 3, 6, and 10) monolayers. The blue-red arrow in the middle of the figure indicates an increasing Te : Mo ratio $R_{\mathrm{Te:Mo}}$ from 1.60 to 1.76, and specific values were written on both sides of the arrow. Specific sizes of the MTB loops and exact Mo and Te ratios are also provided, in which the red (blue) color indicates the most (comparable) stable monolayer, as elucidated later.

ing blocks of MoTe$_{2-x}$ monolayers. The size of an MTB loop is defined by the number (N) of Te$_2$ dimers (denoted Te$_2$-D, balls in light pink) it contains. A triangular loop containing one Te$_2$-D dimer is labeled as $N1$, three as $N3$, and six as $N6$, following the sequence of triangular numbers $\{1, 3, 6, 10, 15, 21, \ldots\}$.

Uniformly sized MTB triangles can be arranged in various configurations, such as vertex-to-vertex or vertex-to-edge. We classify these configurations based on the areas enclosed by the vertices of three MTB triangles. As shown in Fig. 1(b), the vertices of three $N6$ MTB triangular loops form a small triangular area, marked with red dashed triangles, which contains no Te$_2$ dimers and is designated as $T0$, giving rise to the $N6T0$ configuration. In Fig. 1(c), a slightly anticlockwise rotation of the $N6$ loops surrounds an area containing one Te$_2$ dimer (denoted Te$_2$-V, in red), leading to the $N6T1$ configuration. Further rotation encloses three Te$_2$ dimers, forming the $N6T3$ configuration [Fig. 1(d)]. Here, the T value in a monolayer reflects the twist (arrangement) of MTB loops. It is equal to the number of Te$_2$-V dimers and is in the sequence of triangular numbers $\{0, 1, 3, 6, 10, 15, \ldots\}$. The T value must not exceed half of the N value except $N1T1$; for instance, $N10T6$ is meaningless and is equivalent to $N10T3$.

We considered 13 monolayers by varying the sizes ($N1$, $N3$, $N6$, $N10$, $N15$, and $N21$) and arrangements ($T0$, $T1$, $T3$, and $T6$) of the triangular MTB loops (Fig. S3 in the Supplemental Material [54]). The superlattices of these monolayers, with sizes ranging from 12.66 to 30.49 Å, belong to two space groups (SGs): P-62m (No. 189) and P-6 (No. 174). Specifically, the $N1T1$, $N3T6$, and $N6T3$ monolayers crystallize in SG 189 and belong to the D_{3h} point group, which is the direct product of the D_3 point group and a mirror symmetry operation σ_h. Symmetry analysis of their atomic structures (Fig. S3 in the Supplemental Material [54]) suggests these monolayers may form kagome-based lattices, marked with green triangles. The remaining configurations belong to SG 174, associated with point group C_{3h}. Unlike SG 189 monolayers, these monolayers break the mirror symmetry perpendicular to the z axis, resulting in a breathing distortion.

B. Electronic structure of kagome bands

We establish the relationship between atomic structures and electronic properties in these 13 MoTe$_{2-x}$ monolayers by analyzing their band features. We focused on the $T0$ and $T1$ series ($N = 1$, 3, 6, 10, and 15), as the complexity of kagome-related bands in the $T3$ and $T6$ series prevented clear identification of occupied states. For simplicity, spin polarization (SP) was excluded from the analysis so far. Figure 2(a) presents the electronic band structure of $N1T1$ (Mo$_5$Te$_8$ [33]), which forms a coloring triangular (CT) monolayer. Two kagome band sets, KBS1 (red) and KBS2 (blue), are separated by a ~0.1 eV band gap around the Fermi level. These sets exhibit opposite signs for in-plane hopping parameters [62], with the valence band maximum and conduction band minimum positioned at the two (nominal) flat bands, respectively,

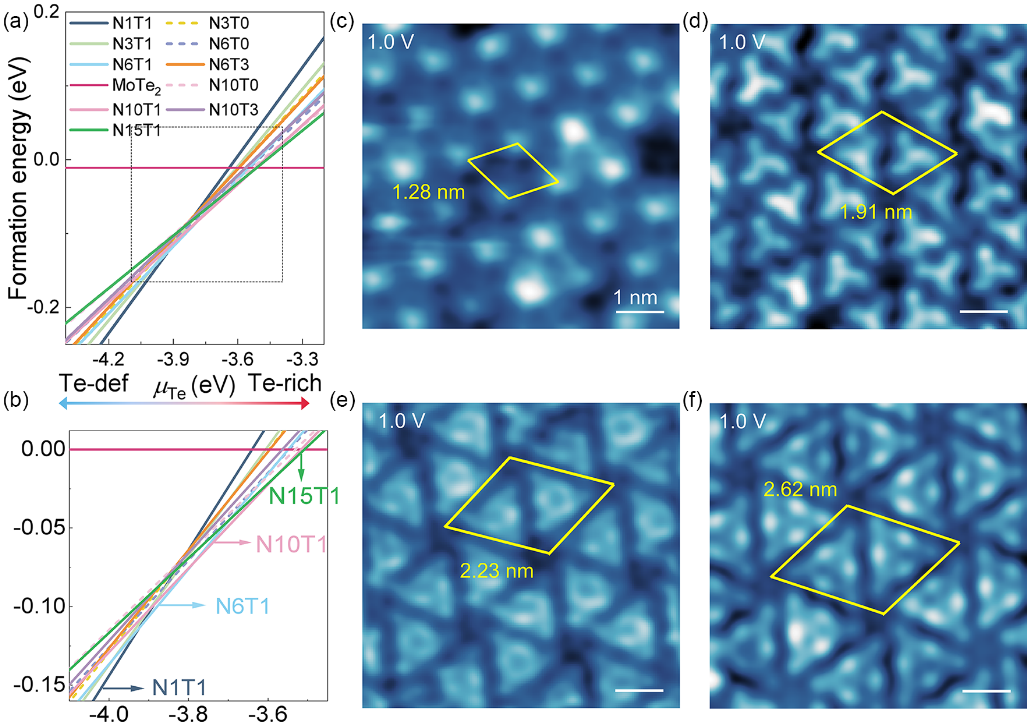

FIG. 3. Formation energies and STM topographic images of different monolayers. (a) Formation energies of the 10 monolayers from Te-deficient to Te-rich conditions without on-site U. (b) The magnified plot of the dashed box area in (a). (c)–(f) STM topography images of $N1T1$, $N6T1$, $N10T1$, and $N15T1$, with the bias voltage of 1.0 V. The yellow rhombuses indicate the supercell of the lattices, with lattice constants shown in yellow digits.

suggesting potential for an exciton insulator [63]. Inclusion of SOC opens a gap between the flat band and a Dirac band at the Γ point of KBS1, as discussed in Fig. S4 in the Supplemental Material [54]. Our calculations yielded Z_2 invariants of 0, 1, and 1 for the three bands of set KBS1 with energies ordered from low to high [marked in Fig. 2(a)], indicating a topological flat band.

The KBS1 set is primarily composed of the out-of-plane Mo-d_{z^2} orbitals, which hybridize with the d_{xy} and $d_{x^2-y^2}$ orbitals at the vertices of MTB loops [Fig. 2(b)], while the KBS2 set mainly arises from Mo-d_{xz} and d_{yz} states at the edges of MTB loops [Fig. 2(c)]. Therefore, the size of the MTB loops (N value) has minimal impact on set KBS1; however, an enlarged size of MTB loops weakens the in-plane confinement and consequently lowers the relative energy levels of KBS2. This trend is confirmed in Figs. 2(d)–2(f), which show the band structures for the remaining $T1$ series with N up to 10. The energy positions of the KBS1 set (red) are nearly unchanged, while those of the KBS2 set (blue) gradually shift downward, leading to partial superposition of the two sets in $N6T1$ and $N10T1$. Notably, this trend invalidates in the $N15$ case [Fig. 2(g)] because a bulk band is occupied after KBS1 and KBS2 are fully filled, as discussed in Fig. S5 in the Supplemental Material [54].

In contrast to the 1:2 ratio in MoTe$_2$, the $T1$ series exhibits progressive reduction in the number of Te atoms, starting with six fewer in $N1T1$ [$\text{Mo}_{15}\text{Te}_{24}(\text{Mo}_5\text{Te}_8)$] and extending to 8, 10, 12, and 14 fewer in $N3T1$ ($\text{Mo}_{23}\text{Te}_{38}$), $N6T1$ ($\text{Mo}_{33}\text{Te}_{56}$), $N10T1$ [$\text{Mo}_{45}\text{Te}_{78}$, ($\text{Mo}_{15}\text{Te}_{26}$)], and $N15T1$ ($\text{Mo}_{59}\text{Te}_{104}$), respectively. This reduction raises the Fermi level to higher energies. By varying the loop size from $N1$ to $N10$, the occupancy of KBS1 and KBS2 (comprising a total of six bands) can be precisely tuned, allowing control over the Fermi level. In $N1T1$ [Fig. 2(a)], the entire KBS1 set is occupied, and in $N3T1$, the flat band of KBS2 becomes pinned at the Fermi level, resulting in a metallic state with a high density of states (DOS) in the spin-degenerated band structure [Fig. 2(d)]. One additional band from KBS2 is filled in $N6T1$ [Fig. 2(e)]; the downward-shifted KBS2 bands partially overlap with the nearly unshifted KBS1 bands, leading to three narrowly distributed bands from the two sets crossing the Fermi level. These three bands, again, lead to a metallic state with a high DOS at the Fermi level. In the $N10T1$ [Fig. 2(f)] and $N15T1$ [Fig. 2(g)] configurations, both KBS1 and KBS2 sets are fully occupied, forming a band insulator state with flat bands near the band edge, showing potential to exhibit emerging states after slightly hole doping.

The $T0$ series exhibits band structure trends similar to the $T1$ series, with the KBS1 set remaining nearly unchanged and the KBS2 set progressively lowering in energy. In the $T0$ series [Figs. 2(h)–2(j)], the KBS2 Dirac bands open an approximately 0.1 eV band gap at the K point for $N3T0$, gradually decreasing to 0.04 eV for $N10T0$. In particular, $N3T0$ and $N6T0$ have a trivial Z_2 index ($Z_2 = 0$), indicating a topologically trivial phase. Three types of band gaps are observed: at a nondegenerate Dirac cone [$N3T0$, Fig. 2(h)], between two KBS sets [$N6T0$, Fig. 2(i)], and at other nondegenerate Dirac cones [$N10T0$, Fig. 2(j)]. The first or third case can be a quantum spin Hall insulator [64,65] if the two Dirac bands are topological nontrivial.

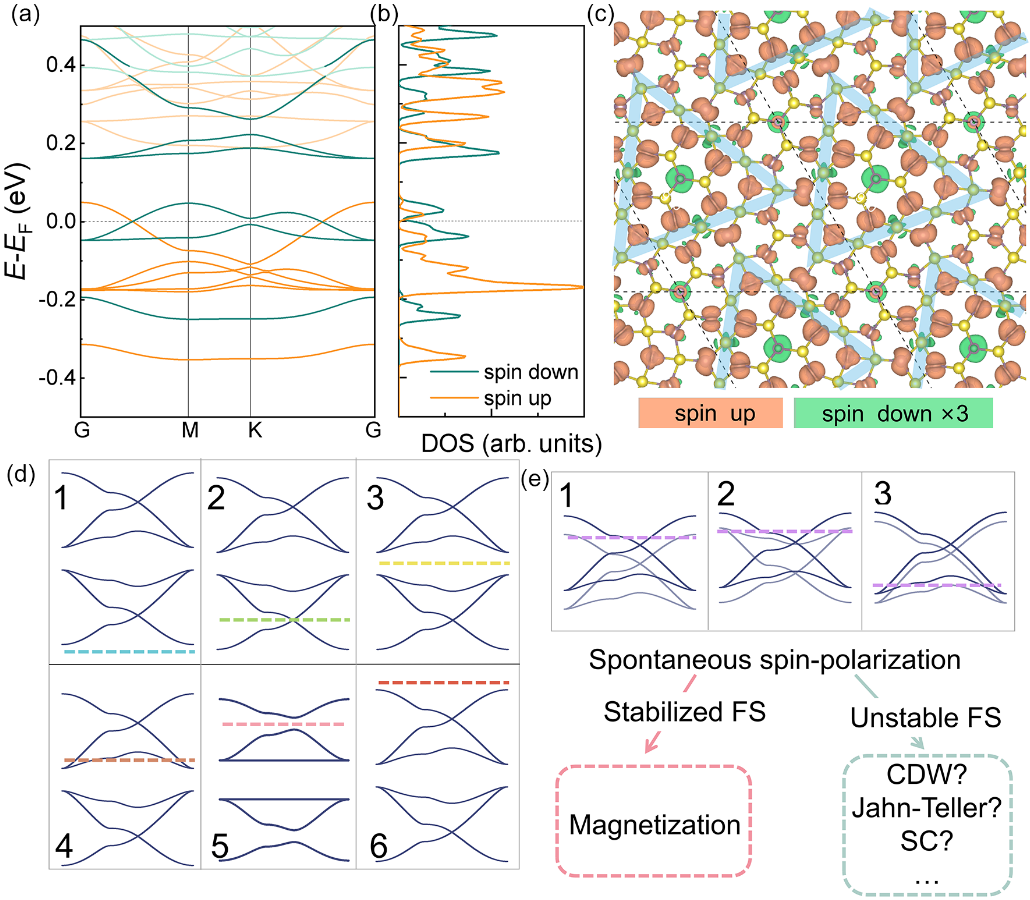

(f)

	Brtg.	SP	Mag. Momt. (μB/Mo)	DI@EF	New Phase	Expt.	Size Theor./Expt. (Å)	NP in Expt.
N1T1	×	×	-	0	-	√	12.7/12.8	×
N3T0	√	×	-	0	-	×	16.6/-	-
N3T1	√	√	0.27	high	likely	×	15.9/-	-
N6T0	√	×	-	0	-	×	20.1/-	-
N6T1	√	√	0.15	high	likely	√	19.2/19.1	√
N6T3	×	√	0.16	high	likely	×	18.8/-	-
N10T0	√	×	-	0	-	×	23.6/-	-
N10T1	√	×	-	0	-	√	22.5/22.3	?
N10T3	√	×	-	0	-	×	21.9/-	-
N15T1	√	×	-	0	-	√	25.9/26.2	?

FIG. 4. Band structures and spin densities of FM *N*3*T*1. (a) SP band structures, (b) corresponding DOS, and (c) spin density for *N*3*T*1. Light-blue shadowed triangles indicate the MTB loops. Orange and green colors represent spin-up and spin-down components. The isosurface contours are 2×10^{-3} e/Bohr^3. (d) Six cases of the position of the Fermi level for isolated KBSs. (e) Three cases of partially overlapped KBSs, which can be classified into two categories based on the stability of the FS, potentially leading to the formation of new phases. (f) Different categories for all configurations distinguished by size, symmetry, and magnetization in theory (Theor.) and experiment (Expt.). The magnetic moment (Mag. Momt.) of each magnetic Mo atom is shown in (f).

C. Formation energy and stability

Figure 3(a) shows the formation energies of the 10 MTB configurations as a function of Te chemical potential. Figure 3(b) zooms in on their relative stability, from which we identify that *N*1*T*1, *N*6*T*1, *N*10*T*1, and *N*15*T*1 are the four most stable monolayers within specific ranges of Te chemical potential outside the Te-rich conditions. Notably, all four predicted stable *T*1 monolayers are experimentally realized, as shown in Figs. 3(c)–3(f), providing strong evidence for their stability. Their lattice constants are 12.8, 19.1, 22.3, and

26.3 Å. The experimental MoTe$_{2-x}$ monolayers were grown on substrates, which may cause slight charge transfer or dielectric screening. However, this is not expected to significantly affect the kagome band dispersion or topology, with the primary effect being a rigid shift in the Fermi level. Additionally, we found that *N*3*T*1, *N*6*T*0, and *N*10*T*0 have comparable stability to the most stable monolayers across varying Te concentrations.

D. High-DOS-driven Stoner FM

Spin-nonpolarized calculations for the *N*3*T*1, *N*3*T*6, *N*6*T*1, and *N*6*T*3 monolayers reveal high DOSs at their Fermi levels [Figs. 2(d) and 2(e) and Figs. S7(a) and S7(b) in the Supplemental Material [54]]. The calculated Stoner criteria for them are 1.82, 1.42, 2.79, and 1.32, respectively, suggesting that they can undergo Stoner FM transition to stabilize their Fermi surfaces (FSs). Our DFT calculations confirm that the FM states are more stable, with total energies at least 10 meV/u.c. lower than their nonmagnetic (NM) counterparts. We tested other non-FM configurations and found that, for *N*3*T*1, an antiferromagnetic (AFM) configuration is 14 meV/u.c. higher than the FM state (Fig. S8 in the Supplemental Material [54]), confirming FM as the ground state. While these results are theoretical, future experiments like Kerr rotation or SP STM could confirm them. Figure 4(a) shows the SP band structure of *N*3*T*1, in which both KBSs for the majority spin (spin-up, in orange) are fully occupied, and the spin-down (in green) KBS1 (the lower energy set) set is partially filled. The spin-up KBS2 primarily resides within the gap of spin-down KBS1, exhibiting a fully polarized peak residing from −0.20 to −0.10 eV in SP DOS shown in Fig. 4(b). Two spin-down KBS1 bands cross the Fermi level, exhibiting a pronounced spin-down density within a range from −0.10 to 0.10 eV [Fig. 4(b)]. Figure 4(c) depicts the spin density in the *N*3*T*1 monolayer, revealing that the majority (up) spin is primarily concentrated on Mo atoms at the MTBs, and the minority (down) spin is mainly distributed on those at the vertices and within the domain. This spatial distribution of spin densities is consistent with the spatial contributions of wave functions for the KBS1 and KBS2 sets. The SP band structure for *N*6*T*1 was presented in Fig. 2 of Ref. [66], and that of *N*3*T*6 and *N*6*T*3 is plotted in Figs. S7(c) and S7(d) in the Supplemental Material [54], where characteristics similar to those of *N*3*T*1 appear. Additionally, an even pronounced spin-down DOS peak resides across the Fermi level, implying an emerging state to further stabilize its FS.

IV. DISCUSSION

When the two KBSs are well isolated, the Fermi level can be positioned in various ways relative to their bands: below [case 1 in Fig. 4(d)] or above two Dirac bands (case 6 realized in *N*6*T*0 and *N*10*T*1), across a degenerate (case 2) or nondegenerate Dirac cone (case 5, *N*3*T*0), between two flat bands (case 3, *N*1*T*1), or across a flat band (case 4, *N*3*T*1). These cases can host band, spin Hall, Mott, or exciton insulators. In the case of partially overlapped KBSs [Fig. 4(e)], the Fermi level may intersect with two Dirac bands (case 1, *N*6*T*3), a flat and a Dirac band (case 2, *N*3*T*6 and *N*6*T*1), or two flat bands (case 3), resulting in a significantly high DOS at the Fermi level. Spontaneous SP could reduce this high DOS, leading to magnetization (*N*3*T*1, *N*6*T*1 [66], and *N*6*T*3). However, in some cases, the DOS remains high even after spin splitting, potentially giving rise to correlated states (*N*6*T*1 [66]), CDWs, or other quantum phases. These phases can be further tuned by adjusting the filling factors using experimental techniques such as electrical gating. All considered configurations could be classified according to their sizes (*N*1–*N*15), atomic lattice symmetries [nonbreathing (Non-Brtg.) and breathing (Brtg.)], SP, and the DOS intensity at the Fermi level (DI@EF), as summarized in Fig. 4(f). Notably, the *T*0 series is consistently spin-nonpolarized, while the *T*1 and *T*3 series could be SP. All magnetic monolayers show high SP DOSs at their Fermi levels, suggesting additional quantum phases likely to emerge in these monolayers.

In summary, we investigated the structural and electronic properties of MoTe$_{2-x}$ monolayers with 13 combinations of various triangular MTB-loop sizes and arrangements. We predicted that the stability of MTB monolayers can be tuned for enabling targeted structural growth by modulating the chemical potential of Te. All studied monolayers feature kagome-based structures with at least two sets of kagome bands near the Fermi level. Among them, we observed Stoner FM and suggested many (topological) exotic electronic states. Additionally, we established the relationship of the occupation of kagome bands with the size and arrangement of MTB loops. This relationship allows for precise optimization of the type of band gap and customization of electronic properties of MoTe$_{2-x}$ monolayers. In this work, we provide theoretical insights for further designing, constructing, and tuning electronic structures of monolayer kagome lattices, especially in *H*-phased transition metal dichalcogenides.

ACKNOWLEDGMENTS

We gratefully acknowledge the financial support from the Ministry of Science and Technology (MOST) of China (Grant No. 2023YFA1406500), the National Natural Science Foundation of China (Grants No. 52461160327 and No. 92477205; W.J.), and the Key Research and Development Program of Wuhan (Grant No. 2024060702030152; C.D.Z.). J.D. was supported by the Outstanding Innovative Talents Cultivation Funded Programs 2023 of Renmin University of China. All calculations for this study were performed at the Physics Lab of High-Performance Computing (PLHPC) and the Public Computing Cloud (PCC) of Renmin University of China.

DATA AVAILABILITY

The data that support the findings of this article are not publicly available. The data are available from the authors upon reasonable request.

[1] J.-X. Yin, B. Lian, and M. Z. Hasan, Topological kagome magnets and superconductors, Nature (London) **612**, 647 (2022).

[2] Y. Wang, H. Wu, G. T. McCandless, J. Y. Chan, and M. N. Ali, Quantum states and intertwining phases in kagome materials, Nat. Rev. Phys. **5**, 635 (2023).

[3] G. Venturini, B. C. E. Idrissi, and B. Malaman, Magnetic properties of RMn$_6$Sn$_6$ (R = Sc, Y, Gd−Tm, Lu) compounds with HfFe$_6$Ge$_6$ type structure, J. Magn. Magn. Mater. **94**, 35 (1991).

[4] D. F. Liu, A. J. Liang, E. K. Liu, Q. N. Xu, Y. W. Li, C. Chen, D. Pei, W. J. Shi, S. K. Mo, P. Dudin, *et al.*, Magnetic Weyl semimetal phase in a kagomé crystal, Science **365**, 1282 (2019).

[5] B. R. Ortiz, S. M. L. Teicher, Y. Hu, J. L. Zuo, P. M. Sarte, E. C. Schueller, A. M. M. Abeykoon, M. J. Krogstad, S. Rosenkranz, R. Osborn, *et al.*, CsV$_3$Sb$_5$: A Z_2 topological kagome metal with a superconducting ground state, Phys. Rev. Lett. **125**, 247002 (2020).

[6] C. C. Zhu, X. F. Yang, W. Xia, Q. W. Yin, L. S. Wang, C. C. Zhao, D. Z. Dai, C. P. Tu, B. Q. Song, Z. C. Tao, *et al.*, Double-dome superconductivity under pressure in the V-based kagome metals AV$_3$Sb$_5$ (A = Rb and K), Phys. Rev. B **105**, 094507 (2022).

[7] H. Chen, H. Yang, B. Hu, Z. Zhao, J. Yuan, Y. Xing, G. Qian, Z. Huang, G. Li, Y. Ye, *et al.*, Roton pair density wave in a strong-coupling kagome superconductor, Nature (London) **599**, 222 (2021).

[8] S. Cao, C. Xu, H. Fukui, T. Manjo, Y. Dong, M. Shi, Y. Liu, C. Cao, and Y. Song, Competing charge-density wave instabilities in the kagome metal ScV$_6$Sn$_6$, Nat. Commun. **14**, 7671 (2023).

[9] J. Ge, P. Wang, Y. Xing, Q. Yin, A. Wang, J. Shen, H. Lei, Z. Wang, and J. Wang, Charge-4e and charge-6e flux quantization and higher charge superconductivity in kagome superconductor ring devices, Phys. Rev. X **14**, 021025 (2024).

[10] M. Li, Q. Wang, G. Wang, Z. Yuan, W. Song, R. Lou, Z. Liu, Y. Huang, Z. Liu, H. Lei, *et al.*, Dirac cone, flat band and saddle point in kagome magnet YMn$_6$Sn$_6$, Nat. Commun. **12**, 3129 (2021).

[11] N. Morali, R. Batabyal, P. K. Nag, E. Liu, Q. Xu, Y. Sun, B. Yan, C. Felser, N. Avraham, and H. Beidenkopf, Fermi-arc diversity on surface terminations of the magnetic Weyl semimetal Co$_3$Sn$_2$S$_2$, Science **365**, 1286 (2019).

[12] E. Liu, Y. Sun, N. Kumar, L. Muechler, A. Sun, L. Jiao, S.-Y. Yang, D. Liu, A. Liang, Q. Xu, *et al.*, Giant anomalous Hall effect in a ferromagnetic kagome-lattice semimetal, Nat. Phys. **14**, 1125 (2018).

[13] Q. Wang, Y. Xu, R. Lou, Z. Liu, M. Li, Y. Huang, D. Shen, H. Weng, S. Wang, and H. Lei, Large intrinsic anomalous Hall effect in half-metallic ferromagnet Co$_3$Sn$_2$S$_2$ with magnetic Weyl fermions, Nat. Commun. **9**, 3681 (2018).

[14] F. H. Yu, D. H. Ma, W. Z. Zhuo, S. Q. Liu, X. K. Wen, B. Lei, J. J. Ying, and X. H. Chen, Unusual competition of superconductivity and charge-density-wave state in a compressed topological kagome metal, Nat. Commun. **12**, 3645 (2021).

[15] Y. Hu, X. Wu, B. R. Ortiz, S. Ju, X. Han, J. Ma, N. C. Plumb, M. Radovic, R. Thomale, S. D. Wilson, *et al.*, Rich nature of Van Hove singularities in kagome superconductor CsV$_3$Sb$_5$, Nat. Commun. **13**, 2220 (2022).

[16] M. Jovanovic and L. M. Schoop, Simple chemical rules for predicting band structures of kagome materials, J. Am. Chem. Soc. **144**, 10978 (2022).

[17] S. Gao, *et al.*, Discovery of a single-band Mott insulator in a van der Waals flat-band compound, Phys. Rev. X **13**, 041049 (2023).

[18] B. R. Ortiz, L. C. Gomes, J. R. Morey, M. Winiarski, M. Bordelon, J. S. Mangum, I. W. H. Oswald, J. A. Rodriguez-Rivera, J. R. Neilson, S. D. Wilson, *et al.*, New kagome prototype materials: Discovery of KV$_3$Sb$_5$, RbV$_3$Sb$_5$, and CsV$_3$Sb$_5$, Phys. Rev. Mater. **3**, 094407 (2019).

[19] S. N. Magonov, P. Zoennchen, H. Rotter, H. J. Cantow, G. Thiele, J. Ren, and M. H. Whangbo, Scanning tunneling and atomic force microscopy study of layered transition metal halides Nb$_3$X$_8$ (X = Cl, Br, I), J. Am. Chem. Soc. **115**, 2495 (1993).

[20] X. Cai, L. An, X. Feng, S. Wang, Z. Zhou, Y. Chen, Y. Cai, C. Cheng, X. Pan, and N. Wang, Layer-dependent interface reconstruction and strain modulation in twisted WSe$_2$, Nanoscale **13**, 13624 (2021).

[21] Z. Li, J. Zhuang, L. Wang, H. Feng, Q. Gao, X. Xu, W. Hao, X. Wang, C. Zhang, K. Wu, *et al.*, Realization of flat band with possible nontrivial topology in electronic kagome lattice, Sci. Adv. **4**, eaau4511 (2018).

[22] K. Lee, M. I. B. Utama, S. Kahn, A. Samudrala, N. Leconte, B. Yang, S. Wang, K. Watanabe, T. Taniguchi, M. V. P. Altoé, *et al.*, Ultrahigh-resolution scanning microwave impedance microscopy of moiré lattices and superstructures, Sci. Adv. **6**, eabd1919 (2020).

[23] D. Pei, B. Wang, Z. Zhou, Z. He, L. An, S. He, C. Chen, Y. Li, L. Wei, A. Liang, *et al.*, Observation of Γ -valley moiré bands and emergent hexagonal lattice in twisted transition metal dichalcogenides, Phys. Rev. X **12**, 021065 (2022).

[24] Q. Zheng, C.-Y. Hao, X.-F. Zhou, Y.-X. Zhao, J.-Q. He, and L. He, Tunable sample-wide electronic kagome lattice in low-angle twisted bilayer graphene, Phys. Rev. Lett. **129**, 076803 (2022).

[25] A. Uri, S. Grover, Y. Cao, J. A. Crosse, K. Bagani, D. Rodan-Legrain, Y. Myasoedov, K. Watanabe, T. Taniguchi, P. Moon, *et al.*, Mapping the twist-angle disorder and Landau levels in magic-angle graphene, Nature (London) **581**, 47 (2020).

[26] H. Yoo, R. Engelke, S. Carr, S. Fang, K. Zhang, P. Cazeaux, S. H. Sung, R. Hovden, A. W. Tsen, T. Taniguchi, *et al.*, Atomic and electronic reconstruction at the van der Waals interface in twisted bilayer graphene, Nat. Mater. **18**, 448 (2019).

[27] M. R. Rosenberger, H.-J. Chuang, M. Phillips, V. P. Oleshko, K. M. McCreary, S. V. Sivaram, C. S. Hellberg, and B. T. Jonker, Twist angle-dependent atomic reconstruction and moiré patterns in transition metal dichalcogenide heterostructures, ACS Nano **14**, 4550 (2020).

[28] C. N. Lau, M. W. Bockrath, K. F. Mak, and F. Zhang, Reproducibility in the fabrication and physics of moiré materials, Nature (London) **602**, 41 (2022).

[29] C. R. Woods, F. Withers, M. J. Zhu, Y. Cao, G. Yu, A. Kozikov, M. Ben Shalom, S. V. Morozov, M. M. van Wijk, A. Fasolino, *et al.*, Macroscopic self-reorientation of interacting two-dimensional crystals, Nat. Commun. **7**, 10800 (2016).

[30] J. D. Sanchez-Yamagishi, T. Taychatanapat, K. Watanabe, T. Taniguchi, A. Yacoby, and P. Jarillo-Herrero, Quantum Hall effect, screening, and layer-polarized insulating states in twisted bilayer graphene, Phys. Rev. Lett. **108**, 076601 (2012).

[31] L. Wang, Y. Gao, B. Wen, Z. Han, T. Taniguchi, K. Watanabe, M. Koshino, J. Hone, and C. R. Dean, Evidence for a fractional

fractal quantum Hall effect in graphene superlattices, Science **350**, 1231 (2015).

[32] D. Wang, G. Chen, C. Li, M. Cheng, W. Yang, S. Wu, G. Xie, J. Zhang, J. Zhao, X. Lu, *et al.*, Thermally induced graphene rotation on hexagonal boron nitride, Phys. Rev. Lett. **116**, 126101 (2016).

[33] L. Lei, J. Dai, H. Dong, Y. Geng, F. Cao, C. Wang, R. Xu, F. Pang, Z.-X. Liu, F. Li, *et al.*, Electronic Janus lattice and kagome-like bands in coloring-triangular $MoTe_2$ monolayers, Nat. Commun. **14**, 6320 (2023).

[34] S.-W. Kim, H. Oh, E.-G. Moon, and Y. Kim, Monolayer kagome metals AV_3Sb_5, Nat. Commun. **14**, 591 (2023).

[35] Y. Zhang, Y. Gu, H. Weng, K. Jiang, and J. Hu, Mottness in two-dimensional van der Waals Nb_3X_8 monolayers (X = Cl, Br, and I), Phys. Rev. B **107**, 035126 (2023).

[36] J. Tu, W. Song, B. Chen, Y. Li, and L. Chen, 2D Covalent organic frameworks with kagome lattice: Synthesis and applications, Chem. Eur. J. **29**, e202302380 (2023).

[37] R. Yin, X. Zhu, Q. Fu, T. Hu, L. Wan, Y. Wu, Y. Liang, Z. Wang, Z.-L. Qiu, Y.-Z. Tan, *et al.*, Artificial kagome lattices of Shockley surface states patterned by halogen hydrogen-bonded organic frameworks, Nat. Commun. **15**, 2969 (2024).

[38] J. Wang, Y. Zheng, X. Nie, C. Xu, Z. Hao, L. Song, S. You, J. Xi, M. Pan, H. Lin, *et al.*, Constructing and transferring two-dimensional tessellation kagome lattices via chemical reactions on Cu(111) surface, J. Phys. Chem. Lett. **12**, 8151 (2021).

[39] M. Pan, X. Zhang, Y. Zhou, P. Wang, Q. Bian, H. Liu, X. Wang, X. Li, A. Chen, X. Lei, *et al.*, Growth of mesoscale ordered two-dimensional hydrogen-bond organic framework with the observation of flat band, Phys. Rev. Lett. **130**, 036203 (2023).

[40] M. Telychko, G. Li, P. Mutombo, D. Soler-Polo, X. Peng, J. Su, S. Song, M. J. Koh, M. Edmonds, P. Jelínek, *et al.*, Ultrahigh-yield on-surface synthesis and assembly of circumcoronene into a chiral electronic kagome-honeycomb lattice, Sci. Adv. **7**, eabf0269 (2021).

[41] Q. Tian, S. I. Vishkayi, M. B. Tagani, L. Zhang, Y. Tian, L.-J. Yin, L. Zhang, and Z. Qin, Two-dimensional artificial Ge superlattice confining in electronic kagome lattice potential valleys, Nano Lett. **23**, 9851 (2023).

[42] B. He, T. Guo, G. Jian, L. Baoxing, S. Kongchao, T. Qiwei, Y. Zhengqing, S. Fei, X. Haipeng, G. Yongli, *et al.*, Structural and electronic properties of atomically thin bismuth on Au(111), Surf. Sci. **679**, 147 (2019).

[43] Y.-H. Lin, C.-J. Chen, N. Kumar, T.-Y. Yeh, T.-H. Lin, S. Blügel, G. Bihlmayer, and P.-J. Hsu, Fabrication and imaging monatomic Ni kagome lattice on superconducting Pb(111), Nano Lett. **22**, 8475 (2022).

[44] Q. Wu, W. Quan, S. Pan, J. Hu, Z. Zhang, J. Wang, F. Zheng, and Y. Zhang, Atomically thin kagome-structured Co_9Te_{16} achieved through self-intercalation and its flat band visualization, Nano Lett. **24**, 7672 (2024).

[45] Z.-M. Zhang, B.-C. Gong, J.-H. Nie, F. Meng, Q. Zhang, L. Gu, K. Liu, Z.-Y. Lu, Y.-S. Fu, and W. Zhang, Self-intercalated $1T$-$FeSe_2$ as an effective kagome lattice, Nano Lett. **23**, 954 (2023).

[46] L. Huang, X. Kong, Q. Zheng, Y. Xing, H. Chen, Y. Li, Z. Hu, S. Zhu, J. Qiao, Y.-Y. Zhang, *et al.*, Discovery and construction of surface kagome electronic states induced by p-d electronic hybridization in $Co_3Sn_2S_2$, Nat. Commun. **14**, 5230 (2023).

[47] S. N. Kempkes, M. R. Slot, J. J. van den Broeke, P. Capiod, W. A. Benalcazar, D. Vanmaekelbergh, D. Bercioux, I. Swart, and C. M. Smith, Robust zero-energy modes in an electronic higher-order topological insulator, Nat. Mater. **18**, 1292 (2019).

[48] Z. Zhang, J. Dai, C. Wang, H. Zhu, F. Pang, Z. Cheng, and W. Ji, 2D kagome materials: Theoretical insights, experimental realizations, and electronic structures, Adv. Funct. Mater. **35**, 2416508 (2025).

[49] L. Dong, G.-Y. Wang, Z. Zhu, C.-X. Zhao, X.-Y. Yang, A.-M. Li, J.-L. Chen, D.-D. Guan, Y.-Y. Li, H. Zheng, *et al.*, Charge density wave states in $2H$-$MoTe_2$ revealed by scanning tunneling microscopy, Chinese Phys. Lett. **35**, 066801 (2018).

[50] J. Zhang, Y. Xia, B. Wang, Y. Jin, H. Tian, W. K. Ho, H. Xu, C. Jin, and M. Xie, Single-layer Mo_5Te_8—A new polymorph of layered transition-metal chalcogenide, 2D Mater. **8**, 015006 (2021).

[51] J. Hong, C. Wang, H. Liu, X. Ren, J. Chen, G. Wang, J. Jia, M. Xie, C. Jin, W. Ji, *et al.*, Inversion domain boundary induced stacking and bandstructure diversity in bilayer $MoSe_2$, Nano Lett. **17**, 6653 (2017).

[52] W. Zhou, X. Zou, S. Najmaei, Z. Liu, Y. Shi, J. Kong, J. Lou, P. M. Ajayan, B. I. Yakobson, and J.-C. Idrobo, Intrinsic structural defects in monolayer molybdenum disulfide, Nano Lett. **13**, 2615 (2013).

[53] H. Liu, L. Jiao, F. Yang, Y. Cai, X. Wu, W. Ho, C. Gao, J. Jia, N. Wang, H. Fan, *et al.*, Dense network of one-dimensional midgap metallic modes in monolayer $MoSe_2$ and their spatial undulations, Phys. Rev. Lett. **113**, 066105 (2014).

[54] See Supplemental Material at http://link.aps.org/supplemental/10.1103/tmd3-whft for additional information for kagome bands and magnetism in $MoTe_{2-x}$ kagome monolayers.

[55] J. P. Perdew, K. Burke, and M. Ernzerhof, Generalized gradient approximation made simple, Phys. Rev. Lett. **77**, 3865 (1996).

[56] P. E. Blöchl, Projector augmented-wave method, Phys. Rev. B **50**, 17953 (1994).

[57] G. Kresse and J. Furthmüller, Efficient iterative schemes for *ab initio* total-energy calculations using a plane-wave basis set, Phys. Rev. B **54**, 11169 (1996).

[58] J. Klimeš, D. R. Bowler, and A. Michaelides, Van der Waals density functionals applied to solids, Phys. Rev. B **83**, 195131 (2011).

[59] A. A. Mostofi, J. R. Yates, G. Pizzi, Y.-S. Lee, I. Souza, D. Vanderbilt, and N. Marzari, An updated version of WANNIER90: A tool for obtaining maximally-localised Wannier functions, Comput. Phys. Commun. **185**, 2309 (2014).

[60] Q. Wu, S. Zhang, H.-F. Song, M. Troyer, and A. A. Soluyanov, WANNIERTOOLS: An open-source software package for novel topological materials, Comput. Phys. Commun. **224**, 405 (2018).

[61] Z. Pan, T. Jian, H. Zhang, X. Lin, C. Zhu, J. Deng, Z. Cheng, C. Liu, and C. Zhang, Unraveling the multistage phase transformations in monolayer $MoTe_{2-x}$, Appl. Phys. Lett. **125**, 151601 (2024).

[62] J. Gao, Q. Wu, C. Persson, and Z. Wang, IRVSP: To obtain irreducible representations of electronic states in the VASP, Comput. Phys. Commun. **261**, 107760 (2021).

[63] G. Sethi, Y. Zhou, L. Zhu, L. Yang, and F. Liu, Flat-band-enabled triplet excitonic insulator in a diatomic kagome lattice, Phys. Rev. Lett. **126**, 196403 (2021).

[64] C. L. Kane and E. J. Mele, Quantum spin Hall effect in graphene, Phys. Rev. Lett. **95**, 226801 (2005).

[65] C. L. Kane and E. J. Mele, Z_2 Topological order and the quantum spin Hall effect, Phys. Rev. Lett. **95**, 146802 (2005).

[66] Z. Pan, W. Xiong, J. Dai, H. Zhang, Y. Wang, T. Jian, X. Cui, J. Deng, X. Lin, Z. Cheng, *et al.*, Ferromagnetism and correlated insulating states in monolayer Mo$_{33}$Te$_{56}$, Nat. Commun. **16**, 3084 (2025).